CAVITATION IN VORTEX AND MIXING IN STRATIFIED FLUIDS

by

Pranav Mohan

A Thesis

Submitted to the Faculty of Purdue University

In Partial Fulfillment of the Requirements for the degree of

Master of Science in Mechanical Engineering

School of Mechanical Engineering

West Lafayette, Indiana

May 2022

THE PURDUE UNIVERSITY GRADUATE SCHOOL

STATEMENT OF COMMITTEE APPROVAL

Dr. Pavlos Vlachos, Chair

School of Mechanical Engineering

Dr. Sadegh Dabiri, Chair

School of Agricultural and Biological Engineering

Dr. Arezoo Ardekani

School of Mechanical Engineering

Approved by:

Dr. Nicole Key

ACKNOWLEDGMENTS

I would like to thank my advisors Professor Sadegh Dabiri and Pavlos Vlachos for their continued support and guidance throughout this journey. I am also thankful to Professor Arezoo Ardekani for her guidance on the project. This helped me grow my research skills and creativity tremendously. I would also like to thank Yuchen Zhang for providing me and helping me with the Basilisk code. I am immensely grateful to Dr. Javad Eshraghi and Sayantan Bhattacharya for mentoring me and helping me make decisions along the road.

TABLE OF CONTENTS

LIST OF FIGURES

ABSTRACT

Cavitation is ubiquitous in nature and scientific application where it might hinder through noise, vibration or erosion which eventually leads to reduced performance. Similarly, rising bubbles are employed in several industrial applications to homogenize the fluid. This thesis sheds light on special applications of these two phenomena.

Once a bubble has been captured by a vortex core, the low (sometimes negative) pressure in the core causes the cavitation bubble to elongate axially while the radius of the bubble oscillates with time. Three dimensional compressible Navier-Stokes equations with surface tension are numerically solved using an all-mach solver on Basilisk software. The bubble dynamics can be categorised into separate stages: spherical growth, pinching, elongation and fragmentation. As the cylindrical bubble grows, it increases the vortex core radius. The flow and the bubble dynamics are strongly coupled. The effect of changing cavitation number and bubble to vortex size ratio has been explored. The bubble sizes and dynamics at different time steps have also been recorded. When the pressure in the core is negative, the bubble continues to grow axially forming a long tube, which is also observed in experiments.

In oceans, density varies with depth due to varying salinity and temperature gradient, which prevents the vertical exchange of heat, carbon, dissolved oxygen, and nutrients as well as blooms the population of harmful bacteria such as cyanobacteria. The rising motion of a single or cluster of bubbles creates an upflow that can cause homogenization or destratification. Confined bubble columns are used for microelectronic cooling as well as in chemical reactors for mixing stratified fluids without any mechanical agitation or power. To begin realizing this complex multi-phase flow system to better understand mixing, we start with a simplified problem of a single air bubble rising in a confined Hele-Shaw channel. We performed a time-resolved stereoscopic Particle Image Velocimetry (PIV) measurement to characterize the bubble wake. Pure water and varying salt concentration were used to achieve a linear density stratification corresponding to Froude numbers (Fr) ranging from 22.1 to 40.7. Due to the large velocity dynamic range for PIV, we enhanced the signal to noise ratio of our correlation planes with pyramid correlation. We found a significant out of plane velocity component in both homogenous and stratified fluid in the vicinity of the bubble, which was assumed to be negligible in previous studies with confined fluid. The wake of the bubble carries the higher density fluid to the top, which later releases from the wake

to form the reverse jet. This buoyant jet has been characterized for different Fr. Eulerian coherent structures are also considered to describe the flow. The rising bubble generates vortices that shed downstream and decay with varying timescales for different Fr. The difference in the coherent structures and decay coefficient leads to a different level of mixing with Fr. The scope of this research is in applications homogenizing the stratified flow using rising bubbles.

1. INTRODUCTION

1.1 Cavitation in vortex

If the circulation velocity of the vortex is high enough, the pressure inside the vortex can reach below vapour pressure, thus causing it to cavitate. With nucleation sites present inside the vortex, bubbles form and grow in a cylindrical shape. The radial velocity creates a shear force that pinches the bubble to grow along the axial direction. During the collapse phase, re-entrant jets form and shock waves propagate radially. This rapid energy dissipation is the cause of damage of various turbomachinery. For this problem, the Reynolds number is to the scale of 105 and thus, the coupled interaction of the vortex and bubble helps us further our understanding of turbulent flows. In fact, cavitating vortices can give rise to turbulence structures.

Due to high non-linearity in the system, the numerous parameters in the system are difficult to control, which is why it is hard to scale vortex cavitation. It has been found that various water quality effects affect the bubble dynamics also (Arndt & Maines, 1994). Tip vortex cavitation takes place when a hydrofoil is placed in high Reynolds number flows (Arndt et al., 1991). By varying the angle of attack, Reynolds number, cavitation number or gas content in water, they found the trajectory of the vortex to be the same, thus making scaling difficult. They also found the pressure to fluctuate at the center of the tip vortex going downstream. Choi et. al. generated a Gaussian vortex in the venturi by passing water over a hydrofoil (Choi & Ceccio, 2007). Using a hydrophone, they found strong acoustic waves being emitted during the collapse process. Also, they did not find the process to scale with the various conventional parameters, such as cavitation number, vortex core size and bubble size. They noted the bubble shape, however, the flow surrounding the bubble and how the vortex changes due to cavitation was not analysed.

Another method is to induce a vortex in the computational domain and place nucleation sites to grow. Using this method Choi et. al. analysed the growth and collapse of the bubble separately (Choi et al., 2009). An advantage of this method is that different kinds of vortices, even the ideal cases such as Rankine vortex, can be studied. To study the bubble dynamics in the simplest case, the second method is employed in this paper. Cavitating vortices have been studied quite thoroughly, however, the bubble dynamics at the core has not received as much attention. Choi et. al. used axisymmetry and incompressible assumptions to predict the length and radius of the bubble, which were 1.5 to 2.0 times higher than from experiments. They show that the radial and

axial motion of the bubble is strongly coupled with the flow surrounding it (Choi et al., 2009). In this paper, the numerical methods are described in Section 2.1 and the setup in Section 2.2. The results are presented in Section 0 followed by some proposed future work in Section 4.1.

1.2 Mixing in Stratified Fluids

Stratification is present in oceans or waterbodies due to a variation in salinity or temperature, which prevents the transport of heat, carbon, oxygen, and nutrients (Li et al., 2020). Stratification also blooms the population of cyanobacteria which can cause conjunctivitis, rhinitis, and among other infections in humans. Moreover, global patterns show that the level of stratification has increased over the last 70 years. Motion of particles, drops and bubbles through stratifications can mix the fluid, which is why this field has received ample interest recently from the research community (Ardekani et al., 2017; Magnaudet & Mercier, 2020; Risso, 2018). In several industrial applications such as chemical reactors and waste processors, stratification could be present through a gradient in temperature, viscosity, or density. Passing particulates, such as drops, particles or bubbles, through these immiscible interfaces or miscible layers, leads to mixing and destratification (Alméras et al., 2013a; Magnaudet & Mercier, 2020). Moreover, stratification leads to a drag enhancement for rising drops and reverse buoyant jet trails behind them (Bayareh et al., 2013a). These effects can be amplified when considering the rise of multiple bubbles. Ganesh et al. conducted a numerical investigation to study mixing due to multiple bubbles rising in stratified fluids and found that as the stratification increases, mixing efficiency increases (Ganesh et al., 2020).

When a bubble rises through an unbounded stratified fluid, mixing occurs due to diffusion, bubble-induced turbulence dispersion, and bubble wake transport (Alméras et al., 2015). The main cause of mixing in a confined domain is due to the bubble wake transport; thus, we perform our experiment in a Hele-Shaw cell to isolate and study the bubble wake transport in more detail (Alméras et al., 2013a; Roig et al., 2012a). The wake length and the vertical bubble velocity decrease with confinement, and the vortex shedding is damped due to the shear stress near the wall leading to negligible turbulence effects (Wang et al., 2016). The horizontal velocity fluctuations originate from the oscillations of the bubble, and the vertical velocity fluctuations come from the wake transport, leading to mixing (Bouche et al., 2014).

Roudet et. al. performed a 2-dimensional 2-component Particle Image Velocimetry (2DPIV) in an emptying narrow channel with Re<200 and a rising bubble of Re=2800 to conclude that this method provides accurate averaged velocities across the depth of the confined channel. However, in this confined domain, Pavlov et al. showed that there can be three dimensionalities when a bubble rises in homogenous fluid (Pavlov et al., 2021a).Thus, we performed stereoscopic PIV to verify if our experiments also show significant out of plane velocity in both homogenous and stratified fluid.

The present study conducts a series of experiments in different stratifications with an objective to shed more light on the three-dimensionality of the flow, formation and evolution of the bubble wake, release and decay of coherent structures, and mixing. To the best of authors' knowledge, no other literature exists studying a single bubble rising through a confined stratified column, and this work reveals the flow structures and liquid dynamics of an oscillating bubble rising in confined stratified fluid for the first time.

2. VORTICAL CAVITATION

2.1 Numerical Methods

Basilisk is an open-source software to solve partial differential equations with adaptive mesh. An "all-mach" solver on Basilisk solves the compressible Navier Stokes (NS) equations in the presence of the viscous and surface tension terms. During cavitation, the rapid changes in pressure can create pressure waves and localized density changes, thus a need for a compressible NS solver. At every time step, an evolution equation for pressure is also solved. This is derived by combining the energy and continuity equation noted in (Fuster et al., 2011). Finally, the system is closed with an equation of state to establish a relationship between different thermodynamic variables such as pressure, temperature and density. A detailed description of the numerical method can be found in the paper by (Fuster & Popinet, 2018).

2.2 Numerical Setup

For the most basic case, a Rankine vortex was induced in a cubic Cartesian domain. For simplicity, an axisymmetric Rankine vortex velocity (u) is given as

$$u_\theta(r) = \frac{\Gamma r}{2\pi r_v^2} \qquad r \le r_v$$
$$u_\theta(r) = \frac{\Gamma}{2\pi r} \qquad r > r_v \qquad \text{Eq 1}$$

Where Γ is the circulation velocity, r is the radius and r_v is the vortex radius. This equation can be plugged into the continuity and NS equations to find an equation for pressure in the computational domain as

$$P = \begin{cases} P_{atm} - \frac{\rho_{atm}\Gamma^2}{4\pi^2 r_v^2} + \frac{\rho_{atm}\Gamma^2 r^2}{8\pi^2 r_v^4} & r \le r_v \\ P_{atm} - \frac{\rho_{atm}\Gamma^2}{8\pi^2 r^2} & r > r_v \end{cases}, \qquad \text{Eq 2}$$

where P_{atm} is the atmospheric pressure and ρ_{atm} is the atmospheric density. Finally, the density at every point can be specified using the following equation of state

$$\rho = \rho_{atm}\left(\frac{\frac{P}{P_{atm}} + B}{1 + B}\right)^{\frac{1}{\gamma}}, \qquad \text{Eq } 3$$

where γ is the heat capacity ratio (γ_{air}=1.4 and γ_{water}=7.15) and B is an empirical constant (B_{air} = 0 and B_{water} = 3049.13. After converting Eq 1-3 to cartesian coordinates, the initial conditions of a Rankine vortex were specified in the solver. The initial air bubble pressure was specified at 1atm and density at 1.2kgm$_{-3}$.

Several dimensionless parameters are also relevant to the numerical simulation. These include cavitation number, $\sigma = \frac{P_{b,0} r_v^2}{\rho_\infty \Gamma^2}$, bubble to vortex size ratio, $r_{bv} = \frac{r_b}{r_v}$ and aspect ratio, which we define as the radius divided by the half length of the bubble. Here, $P_{b,0}$ is the initial pressure inside the bubble which is 1atm and r_b is the bubble pressure. For the cases we are studying here, the bubble will remain axisymmetric. The origin is at the center of the bubble. The axisymmetry is checked by finding the maximum and minimum node in x direction and making sure that this value is the same as maximum and minimum node in y direction. In the simulations, the value of surface tension was kept constant for all simulations as 0.072Nm^{-1}.

2.3 Numerical Validation

Before the code is further modified to fit the necessary boundary and initial conditions, it was first validated. The validation was first conducted to check whether the inviscid equations of shock tube are satisfied.

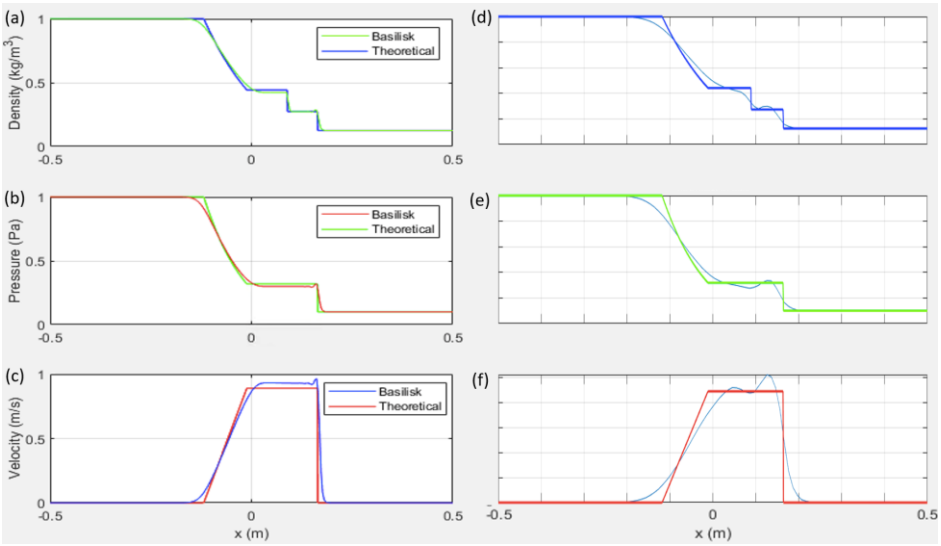

Figure 1: Validation study with the viscous shock tube problem. Here pressure and the density at the left boundary is 1Pa and 1kgm-3 and on the right boundary is P=0.1Pa and ρ=0.125kgm-3. The initial condition in the domain is U=0(m/s). (a,b,c) show the results for N=256 and (d,e,f) show the results N=64.

At N=64 shown, a finer grid size is required and the errors are quite obvious. At N=264, we get a much better agreeance between the Basilisk and theoretical results. Moreover, we also compare the solver against a single cavitation bubble collapse as shown in Figure 2. The Basilisk results do not match exactly the Gilmore and Rayleigh-Plesset equation (RPE) because RPE does not account for liquid compressibility and Gilmore equation even though accounts for compressibility, it does not account for surface tension. Basilisk produces the collapse of a bubble where its intensity reduces in every oscillation.

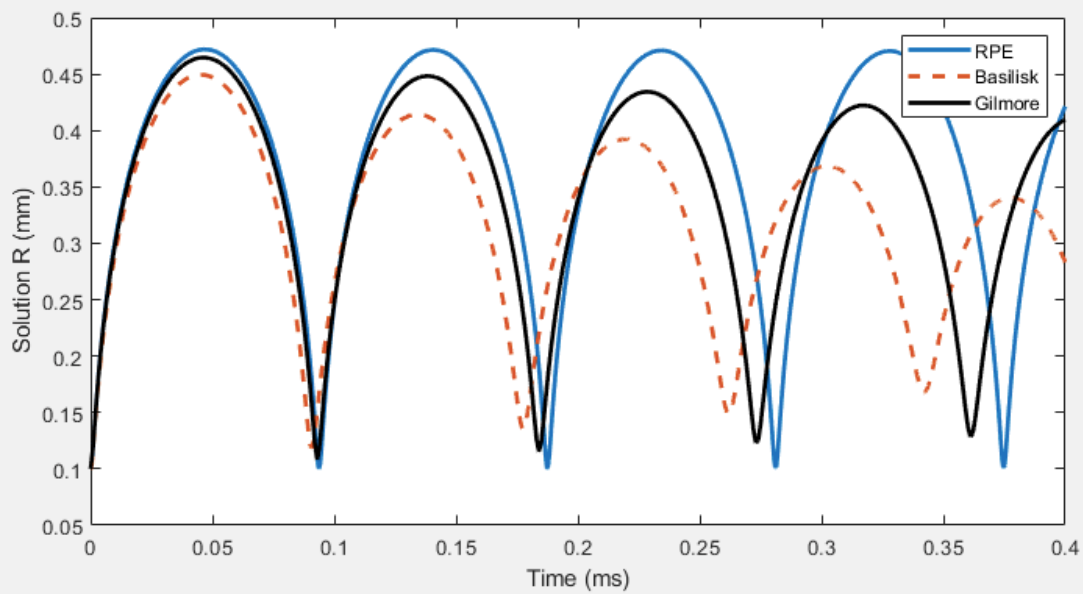

Figure 2: Comparison of the all-mach Basilisk solver with a cavitation bubble collapse simulation.

Finally, we induce a strong vortex with σ=1/200 and observe how it diffuses, which is shown in Figure 3. Performing this is important because we plan to place a nucleation site in the vortex for the same time period and observe the bubble dynamics. In figure Figure 3a and c, we observe how the pressure in the core of the vortex dips and is negative. Over the course of 10ms, this vortex diffuses. The change in velocity and pressure along the x axis is shown in b and d. These results confirm that the we can place a nucleation site in the vortex and assume that the diffusion effects are negligible.

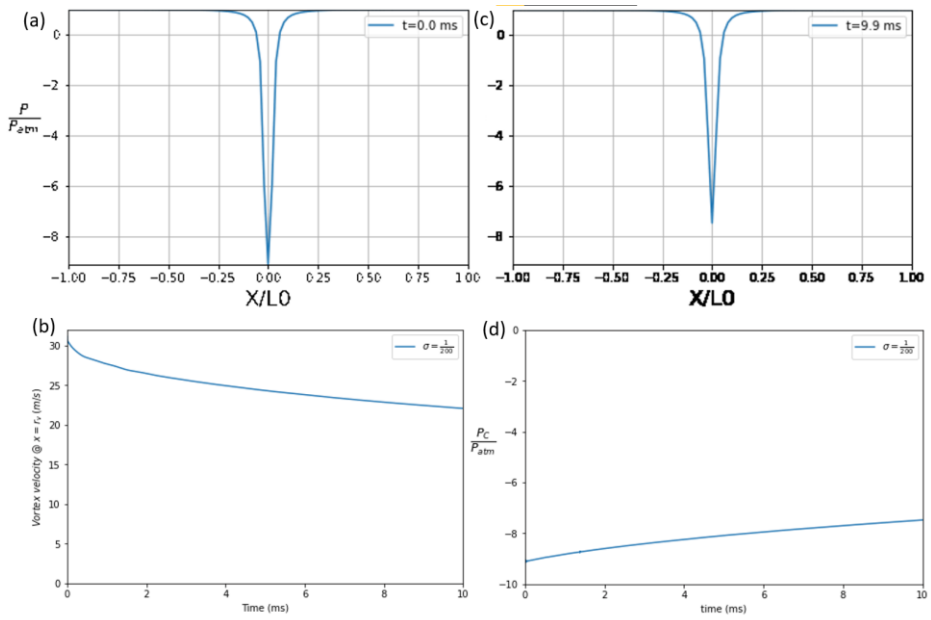

Figure 3: Vortex diffusion at σ=1/200. (a,c) show the Pressure along the x=0 line at time =0ms and 9.9ms. The decrease in vortex velocity and pressure is shown in (b,d)

2.4 Results

Different values of dimensionless parameters were changed by varying the Γ and r_b. Higher Γ means higher circulation velocity and also lower pressure in the core of the vortex. The all-mach solver was validated by simulating the vortex without a bubble and ensuring that the velocity and pressure generated in the 3D domain matched that of a Rankine vortex specified by Eq 1 and 2. This was discussed in our APS-DFD 2020 presentation (Mohan & Dabiri, 2020).

2.4.1 Effect of Cavitation number

For the different cases discussed here, the cavitation number is relatively less than 1, which means that the ratio between the initial bubble pressure, which is 1atm, and pressure at the core is large. In all the cases discussed here, the pressure at the core is negative. It is to be noted that this definition of cavitation number is derived from the Buckingham Pi Theorem.

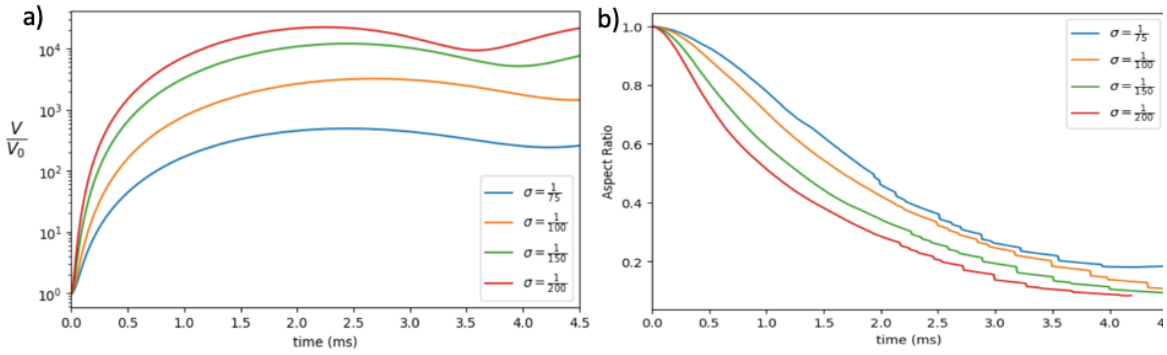

Figure 4: showing the effect of changing cavitation numbers: (a) Semilog plot of volume of the bubble (V) normalized by their initial volume (V0) has been plotted against time; (b) Aspect ratio vs. time

For all the cases demonstrated in the semilog Figure 4, the initial size of the bubble is constant. The volumetric growth of the bubble is 2-4 magnitudes higher than the initial volume of the bubble. As mentioned, the initial pressure inside the air bubble is 1atm which reduces to 0 as the simulations proceed because air pressures cannot be negatives. Cavitation number plays a large role in the simulations as the difference between the smallest and largest cavitation number volume growth considered is of 2 order of magnitude. In Figure 1a, we define the first period as the time period from 0 to the first minima. It is interesting that as the cavitation number increases from 1/200 to 1/100, this first period increases, however, for 1/75 this period decreases. This is further explained in Section 3.3 where the bubble shapes at various points are sketched. Also, from the aspect ratio we observe that the bubble grows spherically initially, for a very short time period. However, due to the pressure difference around the bubble with lower pressures at the core, the bubble grows axially along the core more rapidly than in radial direction. This leads to a cylindrical growth of the bubble as can be seen in Figure 6. This axial growth is stronger in comparison to radial growth in lower cavitation numbers, as can be seen in Figure 4b due to lower aspect ratios. The curves in figure 1b are discontinuous due to the way we defined the aspect ratio and plotting the maximum x and maximum y divided by half z length give overlapping figures.

2.4.2 Effect of bubble to vortex size ratio

The bubble to vortex size ratio was changed by varying the bubble size. It was found that this size of the nucleation site is independent of the bubble dynamics as can be seen in Figure 5. Both the volumetric growth and the aspect ratio remain constant for various ratios. As discussed

in 2.4.1, the bubble initially grows spherically. Thus, before cylindrical dynamics start to take place, the three cases discussed here become similar. Therefore, the nucleation size site is independent of the bubble dynamics that we observe. The zoomed in portion on Figure 5a shows the different initial conditions of the three cases but the solution converges later.

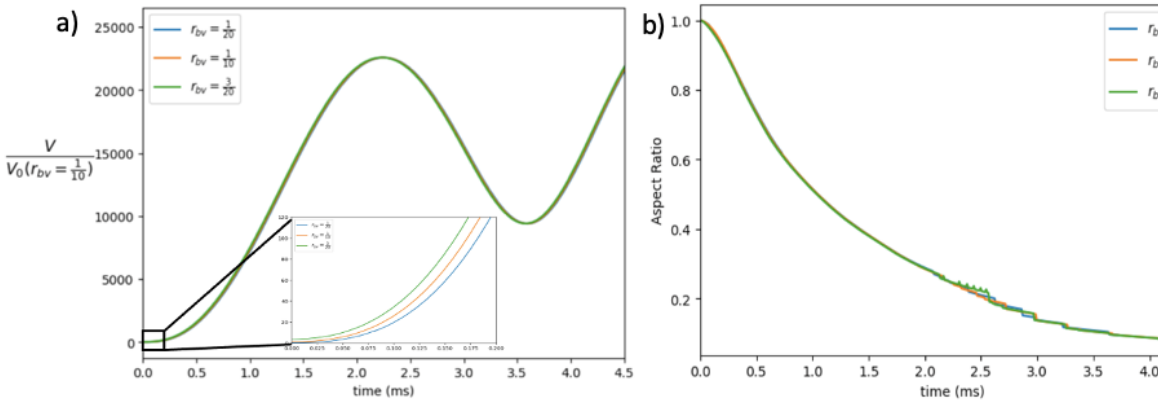

Figure 5: Figure showing the effects of changing bubble to vortex ratio: (a) Volume of the bubble normalized by initial volume of rbc=1/10 for increasing time. A zoomed in figure of the initial time has been shown to indicate different intial conditions; (b) Apect ratio vs. time

2.4.3 Qualitative analysis of the bubble

More details about the bubble dynamics can be inferred by plotting the isosurface of the bubble as shown in Figure 6. Bubble shapes at all the maxima (column 2), minima (column 4) and an intermediate time step (column 1,3) in Figure 4, have been shown in Figure 6. At t=0, the initial bubble size is the same for all the cases. The bubbles shown are to scale, therefore, as also shown through Figure 4, the volumetric growth in lower cavitation number is much larger due to very negative pressure.

The dynamics can be categorized in stages: growth, pinching, elongation and fragmentation. These will be further analyzed in the journal manuscript. In the column 2, the pinching at the center can be observed which is also responsible for the elongation of the bubble in the axial direction. Pinching also leads to a reduction of radius at the center of the bubble and formation of two bubbles separate from the main body on each side in the axial direction. The dynamics observed in cases b-d have similar shapes with the only difference being the size. However, for case a, the bubble at the last time step does not have a similar shape as for other cases. This could be because case a and case b-d fall under different regimes and follow different scaling laws. As discussed in Section

3.1, first period should decrease with decreasing cavitation number but case a does not follow this pattern. To understand this different regime further, we need to run more cases with cavitation numbers in between case a and b.

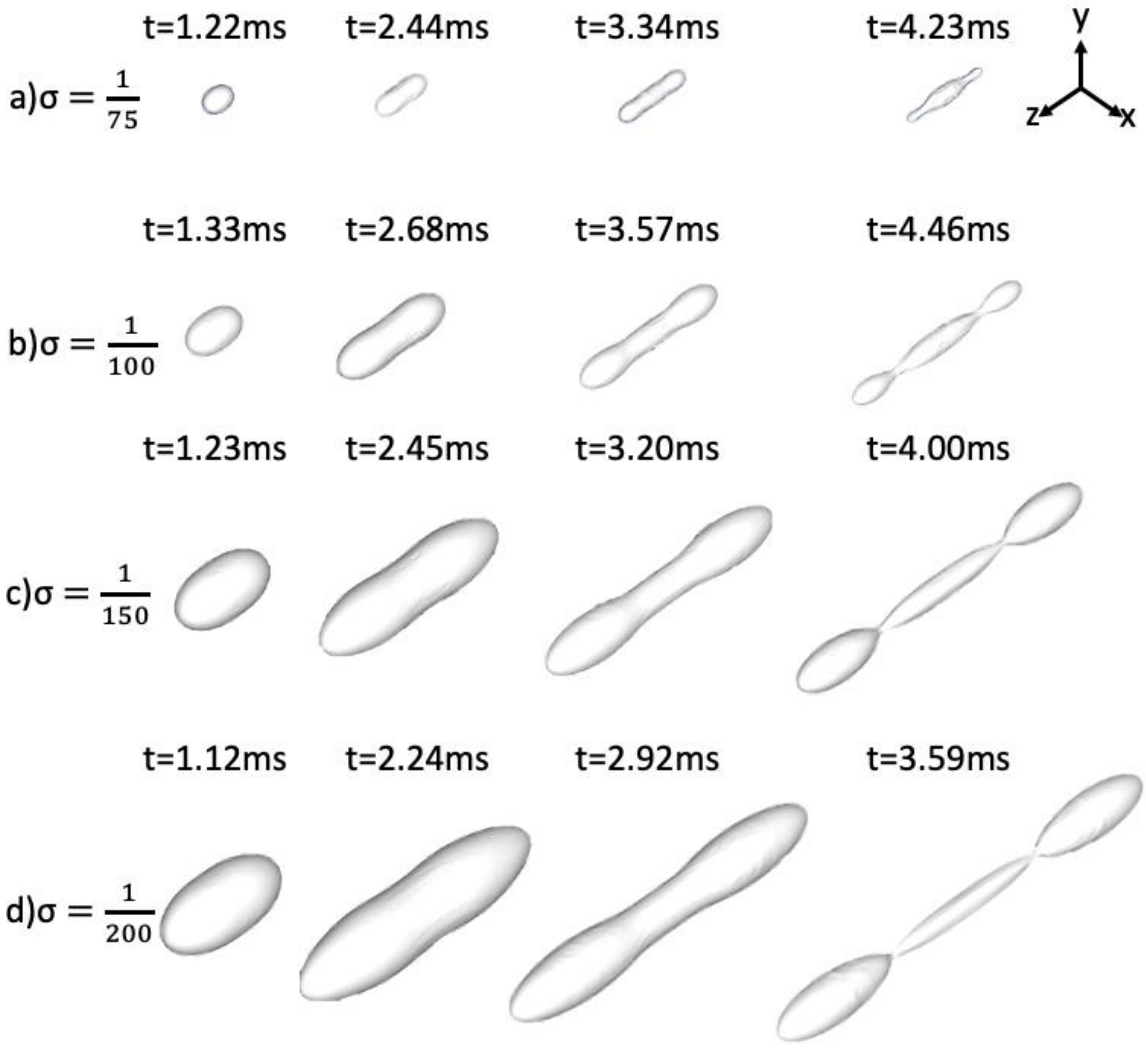

Figure 6: Bubble shapes at different times and cavitation numbers. Column 2 and 4 are maxima and minima from Figure 4 and column 1 and 3 are intermediate times between them. Different rows represent different cavitation numbers

3. MIXING IN STRATIFIED FLUIDS

3.1 Experimental setup and procedure

A single bubble of approximately 3mm diameter is injected from the bottom of a vertical Hele-Shaw column with w=2.5 mm width at a room temperature of 22°C. The acrylic container has a vertical dimension of 0.7m and a breadth of 0.404m. The bubble injector needle is placed at the center of the channel, which is connected to a syringe pump for controlled release of air. The injector has an inner diameter of 0.72mm, which creates the corresponding bubble size. The cameras are placed 0.15m above the position of the needle so that the bubble can reach a steady velocity before entering the field of view.

The experiment was performed in both homogenous and density-stratified liquid. The Double tank forced drain method, introduced by Oster, was used to create the linear density stratification (Economidou & Hunt, 2009a; Oster, 1965). Two tanks are filled with an equal volume of liquid: one with DI water and the other with the salt solution. Two pumps (1 and 2) are required. As discussed in Economidou 2009, by making the flow rate of pump 2 twice that of pump 1, a vertical linear density gradient (β) can be created (Economidou & Hunt, 2009b). The flowrate was measured with Omega, FLR1007-D. Three different solutions are created with densities of 1.192g/cc, 1.291g/cc, and 1.077g/cc. Density was measured using Mettler Toledo, DensitoPro, ±0.001 g⁄cc, and their viscosity was measured with a Rheosense viscometer.

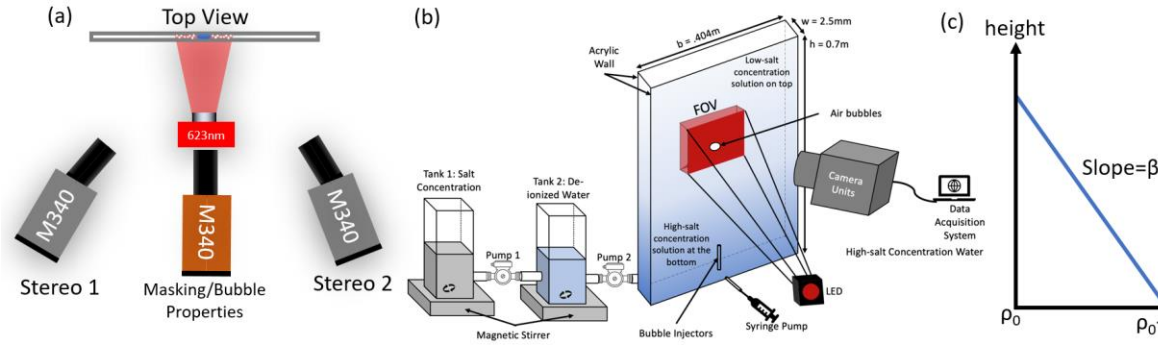

Figure 7: Experimental setup; (a) shows the cameras and the LED from the top view; (b) shows the full experimental setup. Stratification is created using a double-tank forced drain method.

The center camera, shown in Figure 7, was used to record bubble properties which is important in defining several dimensionless quantities of the experiment. The magnification of the center camera was 20.2μm/pixels. Using the bubble images, a segmentation algorithm was created to extract the shape of the bubble as well as other quantities such as velocity and diameter. The bubble image is first binarized using an adaptive threshold of the integral image (Bradley & Roth, 2007). Then an erosion and dilation operations were performed with an window area equal to that of seeded particle image area, which is close to 7pixel^2. Finally, the bubble was detected by finding the connected components using the bwboundaries in MATLAB (MATLAB, 2021). After detecting the bubble boundary, a mask was created where all the pixels inside the bubble boundary are 0 and outside are 1. By extracting the centroid and equivalent diameter, we can evaluate the velocity of the bubble. Since the bubble is elliptical due to being flattened by the wall, equivalent diameter (d_b) is found by $d_b=\sqrt{4A/\pi}$, where A is the area of the bubble and is found to be d_b=3.0±.1mm across all the datasets where the uncertainty is found through the standard deviation between the trials.

Using the mask created, relevant non-dimensionalized parameters such as Reynolds number ($Re=V_b d_b/\nu_f$; 282<Re<463) and Archimedes number ($Ar=\sqrt{gd_b}d_b/\nu_f$; 489<Ar<731) can be calculated, where V_b is the bubble velocity, g is the gravitational acceleration, and ν_f is the mean kinematic viscosity of the stratified fluid. In this study, we are interested in studying the effects of density-stratification on wake dynamics and mixing, which can be characterized using the Froude number ($Fr=V_b/Nd_b$). Here N is the Brunt-Vaïsala frequency ($N=(\beta g/\rho_f)^{.5}$), which signifies the frequency at which an isopycnal oscillates upon being disturbed, and β is the density-stratification in kgm^{-4}. By varying β, we can create a range of stratifications (21.3<Fr<40.2). The homogenous case corresponds to Fr=∞.

A 2D3C stereo-PIV was performed. The fluid is seeded with 20μm polyamide particle with an average density of 1.03g/cc. The field of view was front-illuminated using a Thorlabs SOLIS-525C LED. Three Phantom cameras (Miro 340) were used to sample the images at 500Hz with a resolution of 1600x2560. The images of two side cameras, shown in figure 1, were used in stereo-PIV measurement and they had magnifications of 24μm/pixels and 22.1μm/pixels.

Since the acrylic container, shown in figure 1, is only 2.5mm thick, a calibration plate could not be inserted directly inside the container. Thus, a sliding mechanism was developed where another 1cm wide container adjacent to the Hele-Shaw column was set up. For performing camera

calibration and then recording images, the entire setup was slided back and forth. Calibration was performed on 17 planes with a distance of 0.5mm. ~~5~~ Five ~~different~~ datasets were recorded for each homogenous and three stratified cases. The overlapping region between the two cameras was $11x16d_b$, where d_b is the diameter of the bubble. Post calibration, planar self-calibration was performed from particle images (Wieneke, 2005), and the disparity between frames converged to less than 1 pixel after 4-6 iterations.

The images were preprocessed using minimum image subtraction. When the bubble passes in the field of view, a high dynamic velocity range is observed. This is resolved through pyramid correlations introduced in (Sciacchitano et al., 2012). We used a multi-pass approach with three passes of window resolutions of 48 and 32 pixels. A grid resolution of 16 pixels was chosen, corresponding to 50 points in the wake. To enhance the signal to noise ratio, we performed robust phase correlations (A. C. Eckstein et al., 2008; A. Eckstein & Vlachos, 2009a, 2009b). Finally, the reconstruction from 2D velocity fields was performed using the Soloff method (Prasad, 2000; Soloff et al., 1997).

From the Soloff reconstruction, V_x, V_y, and V_z were obtained on a 2D grid. For Eulerian coherent structures, several options exist, such as Δ criterion (Chong, Perry, and Cantwell 1990), Q criterion (Hunt 1987), and λ_2 (Jeong and Hussain 1995; Chakraborty, Balachandar, and Adrian 2005). However, we chose λ_{CI} which we can obtain both the angle of rotation and the strength of rotation (Chakraborty and Balachandran 2005). The velocity gradients were calculated using a compact Richardson method (Etebari and Vlachos 2005).

3.2 Results

In this section, we highlight the key structures observed in stratified fluids.

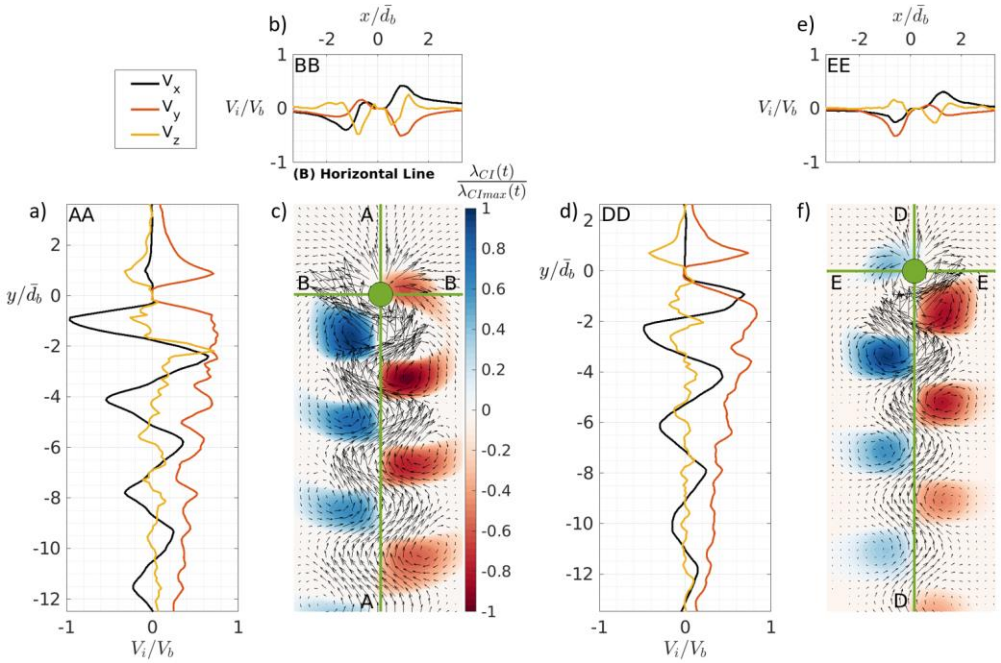

Figure 8: Significance of the out of plane component at Fr=∞, Re=472 (a,b,c) and Fr=21.3, Re=21.29 (d,e,f) near the vicinity of the bubble; (a) shows the normalized velocities across the AA line in c; (b) shows the normalized velocities (Vi where i=x, y, z) across the BB line in c; (c) shows the λCI iso-contours normalized by the maximum λCI at this time and 2D vectors in the field of view at Fr=∞; (d) shows the normalized velocities across the DD line in f; (e) shows the normalized velocities across the EE line in e; (c) shows the λCI normalized by the maximum λCI at this time and 2D vectors in the field of view at Fr=21.3. Skipping 2 vectors for every grid point for better visualization in c and f.

Several studies through the last decade have performed 2D PIV experiments of a single bubble rising in a homogenous fluid to study the wake dynamics (Roig et al. 2012b; Filella, Ern, and Roig 2015a; Alméras et al. 2013b). They assume that the velocity can be averaged over the depth (Roudet et al. 2011). However, recently Pavlov et al. compared the 3-Dimensional 3-Component (3D3C) Shake the Box results with 2DPIV (Pavlov et al. 2021b; Schanz, Gesemann, and Schröder 2016). Through our set of experiments, we want to assess the significance of the V_z in a bubble rising in homogenous, which would confirm the findings of Pavlov et al. and Roudet et al., then we want to assess the significance in stratified fluids, which has never been reported before.

The coherent structures, along with the velocity vectors for a bubble rising in the homogenous fluid, are shown in Figure 8c. The velocity along AA (center y) and BB (center x) lines

is also plotted. In Figure 8a, it is shown that V_z is significant (more than 10% of the bubble velocity) as far as $2.5d_b$ in the wake and $1.5d_b$ in front of the bubble. Similarly, along the line BB, V_z is significant in around $1.5d_b$. Other velocity components, V_x and V_y, remain significant for much longer. Similarly, for stratified fluid (Fr=21.9), the coherent structures and vectors are plotted and the respective velocities at DD and EE are also plotted in Figure 8d, 8e, and 8f. Similar trends as homogenous fluid are found and in stratified fluid where V_z is significant at $2.5d_b$ in the wake and $1d_b$ in front of the bubble. In line EE, Vz is significant $1d_b$. These results are noteworthy it shows a 3D measurement is required when the liquid dynamics close to the bubble is analyzed. However, for any liquid dynamics in the wake of a confined fluid experiment, the out of plane velocity component is negligible. Another observation is that in the stratified fluid, even the V_x becomes insignificant $8d_b$ away, whereas V_y remains significant for much longer. This is due to the vertical flow created by the bubble.

The rising bubble disturbs the isopycnals from their stable neutrally buoyant position. A rising bubble entrains liquid of heavier density in its wake and transports it vertically. When the gravitational force acting on the displaced fluid parcels dominates over its inertia and buoyancy, these parcels return to their original state on a time scale related to 1/N (Bayareh et al., 2013b). It is to be noted that the heavier fluid parcels will advect vertically down and vice versa for lighter fluid parcels. A timeline of V_y over time probed at a center location of the field of view is shown in Figure 9 inset plot. Before the bubble enters the field of view, V_y is 0. When the bubble enters, it creates a positive flow which is why V_y first increases. The bubble then pushes the fluid around it, making the velocity negative. Then, the bubble wake gets dragged upwards making the velocity positive again. At this point, gravitational, buoyancy, and inertial forces are acting on the fluid parcels. The gravitational force starts to dominate, so the velocity goes from positive to negative. The two important locations in this trend are labeled in Figure 9: (i) is when the bubble passes the grid point, (ii) is when the flow reversal begins.

The time scale for the flow reversal (τ_{wake}) given by subtracting the time at point ii from point i in Figure 9a. An average τ_{wake} and its uncertainty is found by considering a spatio-temporal 1D plot at all center y location and by taking the mean and standard deviation of it. It is normalized by the d_b/V_b which is the time scale for the bubble and how quickly the fluid is dragged behind hence it will affect the time at which the flow reversal takes place. Its uncertainty is found from the bubble masking described in section 3.1**Error! Reference source not found.** and is directly

proportional to the Fr with a high R^2 of 0.92. Uncertainty in Fr is calculated through the rms in V_b and d_b. This means that the flow reversal happens faster in stronger stratifications. This is because the isopycnals in stronger stratification are more closely situated and the time scale at which they return to their stable position is given by 1/N. Since 1/N is smaller in higher stratifications, the flow reversal time is shorter. The velocity profile of the jet formed is Gaussian, and a stronger jet is produced when the stratification is stronger (lower Fr).

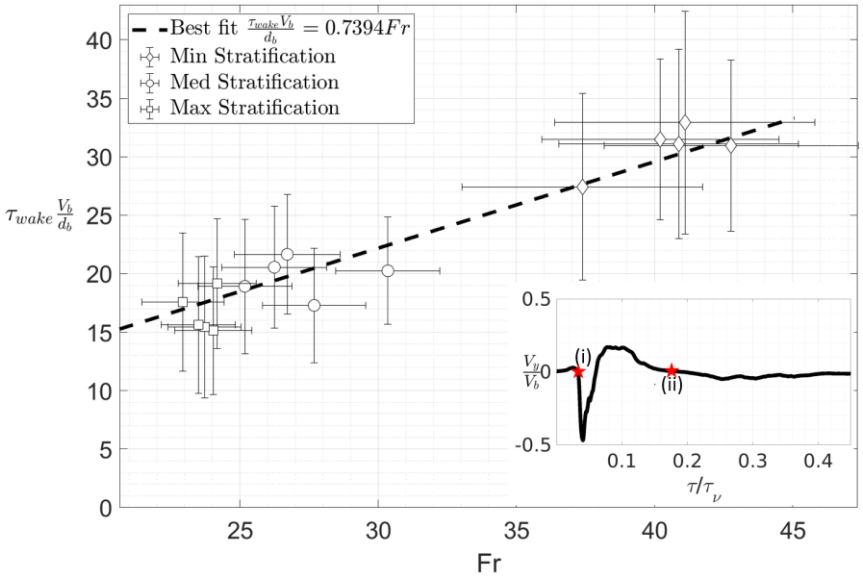

Figure 9: The time scale for flow reversal to begin is plotted against the Fr. Here R2 of the line of best fit is 0.92. Typical Vy over time probed at a center location of the field of view is shown on bottom right. Two points shown here represent (i) when the bubble passes, and (ii) inflection point where the flow reversal begins. Time ii-i gives τwake representing the time scale for when the flow reversal takes place.

Now we turn our attention to the coherent structures that form in the wake shown in Figure 10. As a bubble oscillates while rising, it sheds counter rotating vortices (Figure 10a-f). The Eulerian coherent structures are visualized through λ_{CI} as it provides both the region and rate of rotation in the field of view (Chakraborty et al., 2005). λ_{CI} has been normalized with maximum λ_{CI} at every time step. In homogenous fluid, the vortices get advected upwards due to the upflow created by the bubble, which then come to rest where they dissipate due to the shear stress from the wall and diffuse due to the viscous effect. The time history of the vortex centers shown in Figure 10g-h depict that the vortices travel upwards and then come to rest where they dissipate and diffuse while staying on either side. Similarly, counter rotating vortices are shed behind a rising bubble in the stratified fluid (Figure 11d-f). The wake structure produced at $\tau/\tau_\nu = 0$, where $\tau_\nu = \nu/w^2$, looks similar

for both stratified and homogenous fluid. However, at the intermediate time step $\tau/\tau_\nu = 0.10$ (Figure 11e), the reverse jet begins to form, leading to the coherent structures advecting horizontally as shown through the trajectories time histories in Figure 10i and j. When the vortices begin to dissipate and diffuse, all the counterclockwise rotating vortices (shown in blue) have advected to the right side, and clockwise rotating vortices (shown in red) have advected to the left (Figure 10e and i), which is the opposite to that of homogenous fluid. Moreover, the vortices first get advected upwards reaching a maximum, however, due to the reverse jet, they advect downwards as can be seen in Figure 10j.

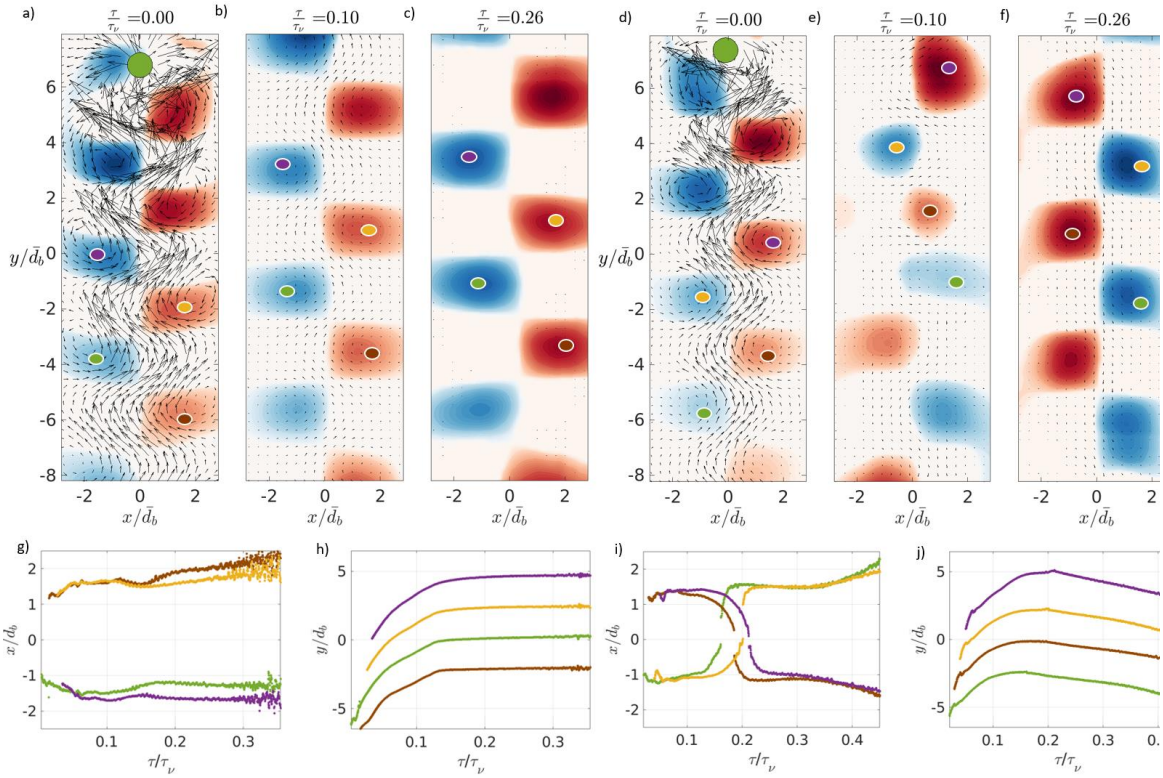

Figure 10: Time evolution of Eulerian coherent structures in homogenous fluid (Fr=∞)(a,b,c) and stratified fluid (Fr=21.9) (d,e,f). λCI is plotted here where it is normalised by the maximum λCI at each time step. The time for every frame is normalised by the viscous time scale given by $\tau_\nu = \nu/w^2$; (g) shows the time history of the horizontal position of the vortices in a-c; (h) shows the time history of the vertical position of the vortices in a-c; i) shows the time history of the horizontal position of the vortices in d-f; (i) shows the time history of the vertical position of the vortices in d-f

Filella et al. have shown the dissipation rate due to shear stress is much higher than diffusion (Filella, Ern, and Roig 2015) when a single bubble rises in confined homogenous fluid. This is because with an exponential viscous decay, we expect the vorticity (Ω_z) to be

$$\Omega_z = \Omega_{z,0}\exp(-12\tau/\tau_\nu), \qquad \text{Eq 4}$$

where Ω_0 is the vorticity at the initial time under the assumption of a parabolic profile in the channel and no inplane diffusion (Roig et al., 2012c). We observe that in homogenous fluid, the vorticity decays at a rate (20) faster than what we expect through diffusion. This is because the vortices interact with the wall and dissipate due to the shear stress. On the semilog Figure 11a, there is a linear decrease in vorticity. Similarly, in stratified fluid (Fr=21.9), the vorticity decreases at the same rate due to the wall shear stress. However, we observe that it becomes constant in the middle (Figure 11b) and then diffuses at a slope of -12. The vorticity becomes constant is unintuitive because a vorticity decay will only be constant when there is energy being supplied into the system which prevents the decay to occur. This energy production term comes from the reverse buoyant jet because of which the vorticity remains constant. Moreover, once the jet velocity reaches close to 0, diffusion occurs and the vortices decay at a rate of -12. We induce that it is because of this reverse jet which causes the vorticity to be sustained for longer which is why we expect the mixing to be higher in stratified fluids.

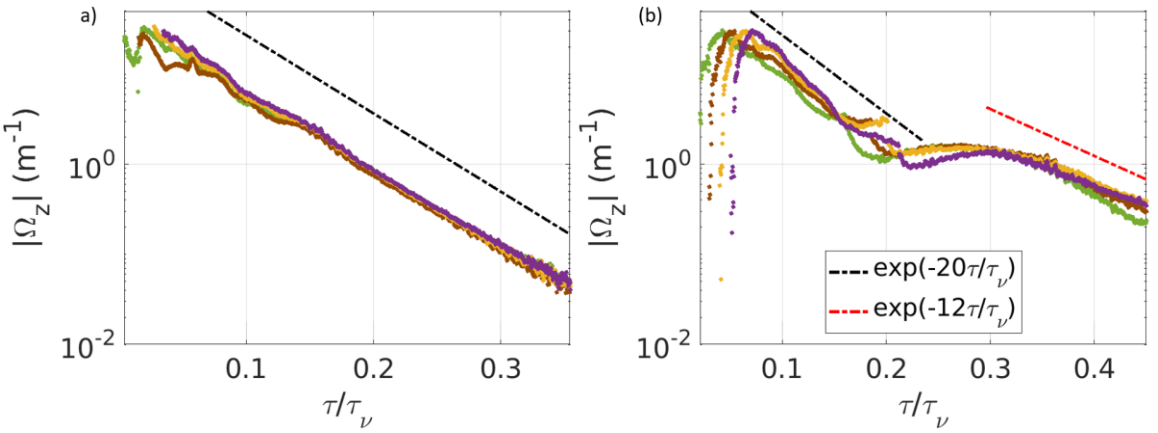

Figure 11: Vorticity decay in homogenous (a) at Fr=∞ and stratified fluid (b) at Fr=21.9. Difference colors represent different vortices from Figure 10. The two slopes shown in black and red represent different decays.

4. CONCLUSION AND FUTURE WORK

4.1 Cavitation in Vortex

Vortex cavitation is a canonical problem that may provide insights into other more complex phenomena. Here, the effect of cavitation number and bubble to vortex radius ratio has been explored. Different scaling laws may apply at different ranges of cavitation numbers. The volumetric growth in lower cavitation numbers is larger and the size of the nucleation site is independent of the bubble dynamics. Here, a brief introduction to the problem has been provided and further work in characterizing different stages of the bubble collapse remain. Various other interesting cases can also be studied such as off-center bubble or a bubble-pair dynamics.

4.2 Mixing in Stratified Fluid

A stereo-PIV experiment is performed to study the wake dynamics of a single bubble rising in homogenous and stratified fluids. The resolved velocity out of plane component (V_z) is shown to be significant in the vicinity of the bubble to around $2.5d_b$ in both homogenous and stratified fluid. However, far away from the bubble, this component becomes negligible due to the shear stresses from the wall. Moreover, as the bubble rises in the stratified fluid, it entrains denser liquid in its wake and transports it vertically. Once the inertia and buoyancy of the denser fluid parcel match that of gravitational force, flow reversal takes place, and these heavier fluid parcels fall. We also find that the time scale for the flow reversal (τ_{wake}) is proportional to Fr. In the coherent structure analysis, we found that the oscillating bubble releases counter-rotating vortices that travel upwards due to the upflow created by the bubble. In homogenous fluid, the vortices travel up and dissipate, whereas, in the stratified fluid, they travel up and then move horizontally at the onset of flow reversal, followed by downward motion due to the reverse jet, which may be the reason for higher mixing efficiency found in stratified fluids. They vortices at first decay due to the shear stress from the wall followed by being constant where they get energy from the reverse jet. Finally, they advect down because of the reverse jet and diffuse. The results from this experimental study can be used to understand mixing due to the wake dynamics of an oscillating bubble in stratified fluids.

REFERENCES

Alméras, E., Risso, F., Roig, V., Cazin, S., Plais, C., & Augier, F. (2015). Mixing by bubble-induced turbulence. *Journal of Fluid Mechanics*, *776*, 458–474.

Alméras, E., Roig, V., Risso, F., Cazin, S., Plais, C., & Augier, F. (2013a). Mixing by a bubbly flow in a Hele-Shaw cell: time-resolved measurements and modelling.

Alméras, E., Roig, V., Risso, F., Cazin, S., Plais, C., & Augier, F. (2013b). Mixing by a bubbly flow in a Hele-Shaw cell: time-resolved measurements and modelling.

Ardekani, A. M., Doostmohammadi, A., & Desai, N. (2017). Transport of particles, drops, and small organisms in density stratified fluids. *Physical Review Fluids*, *2*(10), 100503.

Arndt, R. E. A., Arakeri, V. H., & Higuchi, H. (1991). Some observations of tip-vortex cavitation. *Journal of Fluid Mechanics*, *229*, 269–289.

Arndt, R. E. A., & Maines, B. H. (1994). *Vortex cavitation: A progress report*.

Bayareh, M., Doostmohammadi, A., Dabiri, S., & Ardekani, A. M. (2013a). On the rising motion of a drop in stratified fluids. *Physics of Fluids*, *25*(10), 23029.

Bayareh, M., Doostmohammadi, A., Dabiri, S., & Ardekani, A. M. (2013b). On the rising motion of a drop in stratified fluids. *Physics of Fluids*, *25*(10), 23029.

Bouche, E., Roig, V., Risso, F., & Billet, A.-M. (2014). Homogeneous swarm of high-Reynolds-number bubbles rising within a thin gap. Part 2. Liquid dynamics. *Journal of Fluid Mechanics*, *758*, 508–521.

Bradley, D., & Roth, G. (2007). Adaptive thresholding using the integral image. *Journal of Graphics Tools*, *12*(2), 13–21.

Chakraborty, P., Balachandar, S., & Adrian, R. J. (2005). On the relationships between local vortex identification schemes. *Journal of Fluid Mechanics*, *535*, 189–214.

Choi, J., & Ceccio, S. L. (2007). Dynamics and noise emission of vortex cavitation bubbles. *Journal of Fluid Mechanics*, *575*, 1–26.

Choi, J., Hsiao, C.-T., Chahine, G., & Ceccio, S. (2009). Growth, oscillation and collapse of vortex cavitation bubbles. *Journal of Fluid Mechanics*, *624*, 255–279.

Chong, M. S., Perry, A. E., & Cantwell, B. J. (1990). A general classification of three-dimensional flow fields. *Physics of Fluids A: Fluid Dynamics*, *2*(5), 765–777.

Eckstein, A. C., Charonko, J., & Vlachos, P. (2008). Phase correlation processing for DPIV measurements. *Experiments in Fluids*, *45*(3), 485–500.

Eckstein, A., & Vlachos, P. P. (2009a). Assessment of advanced windowing techniques for digital particle image velocimetry (DPIV). *Measurement Science and Technology*, *20*(7), 75402.

Eckstein, A., & Vlachos, P. P. (2009b). Digital particle image velocimetry (DPIV) robust phase correlation. *Measurement Science and Technology*, *20*(5), 55401.

Economidou, M., & Hunt, G. R. (2009a). Density stratified environments: the double-tank method. *Experiments in Fluids*, *46*(3), 453–466.

Economidou, M., & Hunt, G. R. (2009b). Density stratified environments: the double-tank method. *Experiments in Fluids*, *46*(3), 453–466.

Etebari, A., & Vlachos, P. P. (2005). Improvements on the accuracy of derivative estimation from DPIV velocity measurements. *Experiments in Fluids*, *39*(6), 1040–1050.

Filella, A., Ern, P., & Roig, V. (2015a). Oscillatory motion and wake of a bubble rising in a thin-gap cell. *Journal of Fluid Mechanics*, *778*, 60–88.

Filella, A., Ern, P., & Roig, V. (2015b). Oscillatory motion and wake of a bubble rising in a thin-gap cell. *Journal of Fluid Mechanics*, *778*, 60–88.

Fuster, D., Dopazo, C., & Hauke, G. (2011). Liquid compressibility effects during the collapse of a single cavitating bubble. *The Journal of the Acoustical Society of America*, *129*(1), 122–131.

Fuster, D., & Popinet, S. (2018). An all-Mach method for the simulation of bubble dynamics problems in the presence of surface tension. *Journal of Computational Physics*, *374*, 752–768.

Ganesh, M., Kim, S., & Dabiri, S. (2020). Induced mixing in stratified fluids by rising bubbles in a thin gap. *Physical Review Fluids*, *5*(4), 43601.

Hunt, J. C. R. (1987). Vorticity and vortex dynamics in complex turbulent flows. *Transactions of the Canadian Society for Mechanical Engineering*, *11*(1), 21–35.

Jeong, J., & Hussain, F. (1995). On the identification of a vortex. *Journal of Fluid Mechanics*, *285*, 69–94.

Li, G., Cheng, L., Zhu, J., Trenberth, K. E., Mann, M. E., & Abraham, J. P. (2020). Increasing ocean stratification over the past half-century. *Nature Climate Change*, *10*(12), 1116–1123.

Magnaudet, J., & Mercier, M. J. (2020). Particles, drops, and bubbles moving across sharp interfaces and stratified layers. *Annual Review of Fluid Mechanics*, *52*, 61–91.

MATLAB. (2021). *version 7.10.0 (R2021a)*. The MathWorks Inc.

Mohan, P., & Dabiri, S. (2020). Numerical Simulation of Cavitation Bubble Dynamics in a Rankine Vortex. *APS Division of Fluid Dynamics Meeting Abstracts*, F02–014.

Oster, G. (1965). Density gradients. *Scientific American*, *213*(2), 70–79.

Pavlov, L., Cazin, S., Ern, P., & Roig, V. (2021a). Exploration by Shake-the-Box technique of the 3D perturbation induced by a bubble rising in a thin-gap cell. *Experiments in Fluids*, *62*(1), 1–19.

Pavlov, L., Cazin, S., Ern, P., & Roig, V. (2021b). Exploration by Shake-the-Box technique of the 3D perturbation induced by a bubble rising in a thin-gap cell. *Experiments in Fluids*, *62*(1), 1–19.

Prasad, A. K. (2000). Stereoscopic particle image velocimetry. *Experiments in Fluids*, *29*(2), 103–116.

Risso, F. (2018). Agitation, mixing, and transfers induced by bubbles. *Annual Review of Fluid Mechanics*, *50*, 25–48.

Roig, V., Roudet, M., Risso, F., & Billet, A.-M. (2012a). Dynamics of a high-Reynolds-number bubble rising within a thin gap. *Journal of Fluid Mechanics*, *707*, 444–466.

Roig, V., Roudet, M., Risso, F., & Billet, A.-M. (2012b). Dynamics of a high-Reynolds-number bubble rising within a thin gap. *Journal of Fluid Mechanics*, *707*, 444–466.

Roig, V., Roudet, M., Risso, F., & Billet, A.-M. (2012c). Dynamics of a high-Reynolds-number bubble rising within a thin gap. *Journal of Fluid Mechanics*, *707*, 444–466.

Roudet, M., Billet, A.-M., Risso, F., & Roig, V. (2011). PIV with volume lighting in a narrow cell: An efficient method to measure large velocity fields of rapidly varying flows. *Experimental Thermal and Fluid Science*, *35*(6), 1030–1037.

Schanz, D., Gesemann, S., & Schröder, A. (2016). Shake-The-Box: Lagrangian particle tracking at high particle image densities. *Experiments in Fluids*, *57*(5), 1–27.

Sciacchitano, A., Scarano, F., & Wieneke, B. (2012). Multi-frame pyramid correlation for time-resolved PIV. *Experiments in Fluids*, *53*(4), 1087–1105.

Soloff, S. M., Adrian, R. J., & Liu, Z.-C. (1997). Distortion compensation for generalized stereoscopic particle image velocimetry. *Measurement Science and Technology*, *8*(12), 1441.

Wang, X., Klaasen, B., Degrève, J., Mahulkar, A., Heynderickx, G., Reyniers, M.-F., Blanpain, B., & Verhaeghe, F. (2016). Volume-of-fluid simulations of bubble dynamics in a vertical Hele-Shaw cell. *Physics of Fluids*, *28*(5), 53304.

Wieneke, B. (2005). Stereo-PIV using self-calibration on particle images. *Experiments in Fluids*, *39*(2), 267–280.

PUBLICATIONS

Journal Publications

J2. **Mohan, P.,** Bhattacharya, S., Masoomi, F., Eshraghi, J., Ardekani, A., Dabiri, S., Vlachos, P., "Mixing induced by a single bubble rising in confined stratified fluid." *in prep.*, (2022)

J1. Nellippallil, A. B., **Mohan, P.,** Allen, J. K., and Mistree, F., 2020. "An Inverse, Decision-Based Design Method for Robust Concept Exploration." ASME. *J. Mech. Des*. August 2020; 142(8): 081703. Link**.**

Conference Publications

C7. **Mohan, P.,** Bhattacharya, S., Masoomi, F., Eshraghi, J., Ardekani, A., Dabiri, S., Vlachos, P., "Dynamics of single bubble rising in confined stratified fluid." 20th International Symposium on Applications of Laser and Imaging Techniques to Fluid Mechanics. *submitted.*, (2022)

C6. **Mohan, P.,** Bhattacharya, S., Masoomi, F., Eshraghi, J., Dabiri, S., Vlachos, P., "Dynamics of a single bubble rising in confined stratified flow." Bulletin of the American Physical Society – Division of Fluid Mechanics, Phoenix, AZ, USA. Link, Video

C5. Masoomi, F., **Mohan, P.,** Bhattacharya, S., Eshraghi, J., Ardekani, A., Dabiri, S., Vlachos, P., "Dynamics of a single bubble rising in confined stratified flow." Bulletin of the American Physical Society – Division of Fluid Mechanics, Phoenix, AZ, USA. Link, Video

C4. **Mohan, P.,** Dabiri, S., "Cavitation bubble dynamics in a line Rankine vortex." 11th Symposium on Cavitation (CAV2021), 2021, Video

C3. **Mohan, P.,** Dabiri, S., 2020, "Numerical Simulation of Cavitation Bubble Dynamics in a Rankine Vortex." Bulletin of the American Physical Society – Division of Fluid Mechanics, Chicago, IL, USA. Link, Video

C2 Nellippallil, A.B., **Mohan, P.**, Allen, J.K., and Mistree, F., 2019, "*Inverse Thermo-Mechanical Processing (ITMP) Design of a Steel Rod During Hot Rolling Process*," ASME Design Automation Conference, Anaheim, CA, USA. Paper Number: DETC2019-97930. Link**.**

C1 Nellippallil, A.B., **Mohan, P.**, Allen, J.K., and Mistree, F., 2018, "*Robust Concept Exploration of Materials, Products and Associated Manufacturing Processes*," ASME Design Automation Conference, Quebec City, Canada. Paper Number: DETC2018-85913. Link**.**

Posters and Presentations

P12. **Mohan, P.,** Bhattacharya, S., Masoomi, F., Eshraghi, J., Ardekani, A., Dabiri, S., Vlachos, P., "Mixing induced by a single bubble rising in confined stratified fluid." *Graduate Industrial Research Symposium* (2022)

P11. **Mohan, P.,** Anilkumar, A., Akhras, A., Junus, F., Narsimhan, P., Chen J., Takahashi, G., Brophy, S., Vlachos, P., Bane, S., "miFluidsLab: Multi-modal Interactive Fluids Laboratory," Annual Graduate Student Education Research Symosium (AGSERS) 2022

P10. **Mohan, P,** Belardo, C.,7th February 2020, "Menstrual Cups for Women Empowerment: A research study in Northern India," ABE Graduate Research Symposium, West Lafayette, Indiana, USA

P9. Belardo, C., **Mohan, P.**, Yadav, A., Allen, J. K.,1st November 2019, "Menstrual Cups for Women Empowerment: A research study in Northern India," Women's Health Symposium, West Lafayette, Indiana, USA

P8. **TEDxOU** – Belardo, C. R., **Mohan P.**, "Menstrual Cup for Women Empowerment," University of Oklahoma, Norman, USA, 13th September 2019 - Link

P7. **Undergraduate Research Day 2019** – Belardo, C. R., **Mohan, P.**, Allen, J. K., Mistree, F., "Menstrual Cups for Women's Empowerment," University of Oklahoma, Norman, USA, 6th April 2019

P6. **Undergraduate Research Day 2019** – **Mohan, P.,** Mandal, S., Nellippallil, A. B., Cavieres, A., "Moving Failure Analysis to Early Stages of Design with FMEA and Additive Manufacturing," University of Oklahoma, Norman, USA, 6th April 2019

P5. **Undergraduate Research Day 2018 – Mohan, P.,** Nellippallil, A.B., Allen, J.K., Mistree, F., "Microstructural Modelling of Hot Rod Rolling using Inverse Goal-Oriented Decision Based Design Method," University of Oklahoma, Norman, USA, 7th April 2018

P4. **Symposium Presentation** – **Mohan, P.,** Nellippallil, A.B., Allen, J.K., Mistree, F., "Microstructural Modelling of Hot Rod Rolling using Inverse Goal-Oriented Decision Based Design Method," American Institute of Aeronautics and Astronautics and American Society of Mechanical Engineers (AIAA & ASME Symposium), 14th April, 2018

P3. **Mohan, P.,** Nellippallil, A.B., Allen, J.K., Mistree, F., 5th March 2018, "A Goal-Oriented, Inverse Decision Based Design Method to Achieve the Vertical and Horizontal Integration of Models", Student Research and Creativity Day, National Weather Center, University of Oklahoma, Norman, USA

P2. **Mohan, P.**, Nellippallil, A.B., Allen, J.K., Mistree, F., 12th August 2017, "Staying Competitive with IGODBD and Sustainable Manufacturing", IDETC 2017, Cleveland, Ohio, USA

P1. **Mohan, P.,** Nellippallil, A.B., Allen, J.K., Mistree, F., 8th April 2017, "A Goal-Oriented, Inverse Decision Based Design Exploration of a Multistage Hot Rod Rolling System", Undergraduate Research Day 2017, Honors College, University of Oklahoma, Norman USA